Metal-Free Benzothioxanthene Imide Based Dyes for Organic Light-Emitting Electrochemical Cells

Kwang Keat Leong, Hee Jung Kim, Korentin Morice, Pierre Josse, Darío Puchán Sánchez, Jinbo Kim, Yanghyun Auh, Donghwan Kim, Philippe Blanchard, Cyrille Monnereau, et al.

ADVANCED OPTICAL MATERIALS
www.advopticalmat.de

Metal-Free Benzothioxanthene Imide Based Dyes for Organic Light-Emitting Electrochemical Cells

Kwang Keat Leong, Hee Jung Kim, Korentin Morice, Pierre Josse, Darío Puchán Sánchez, Jinbo Kim, Yanghyun Auh, Donghwan Kim, Philippe Blanchard, Cyrille Monnereau, Clément Cabanetos,* and Eunkyoung Kim**

Two synthetic organic dyes of the Benzothioxanthene imide (BTI) family are explored as a promising electroactive material for organic light-emitting electrochemical cells (LECs). The high thermal stability and ease of thin film processing make BTI-based compounds suitable for these devices. However, their planar π-conjugated structure often leads to aggregation-caused quenching (ACQ), reducing luminescence in the solid state. To overcome this, this study has taken advantage of host-guest interactions with 4,4′-bis(9H-carbazol-9-yl) biphenyl (p-CBP), poly(9-vinylcarbazole) (PVK), and poly(dioctylfluorene) (PFO) to suppress ACQ. The use of p-CBP improved the internal electrical double layer (EDL) alignment within the film, resulting in higher luminescence compared to PFO and PVK-based LECs. The BTI-F dye, when incorporated into a dual host system with p-CBP and PFO, achieved an impressive luminescence of up to 3900 cd m^{-2}. Additionally, PFO enhanced charge balance, contributing to a blue shift in maximum absorption wavelength and increasing the device's tolerance. A triple-host system (p-CBP, PVK, PFO) further extended the device's half-life ($t_{1/2}$) to 54 min, demonstrating the potential of these host-guest systems in advancing metal-free LEC technology.

1. Introduction

Due to their ease of fabrication, organic light-emitting electrochemical cells have attracted considerable research attention over the last few decades.[1] Light-emitting electrochemical cell (LEC) devices, consisting of an active layer sandwiched between two electrodes, offer the unique advantage of being compatible with the use of moisture and air-stable cathodes, thus avoiding stringent protection from molecular water and oxygen contamination. Characterized by their high brightness and ease of preparation, transition-metal complexes (mainly ruthenium or iridium) are still the most commonly used small molecular active materials even though they are among the most expensive elements and raise environmental concerns.[2–7] In this context, several synthetically accessible organic dyes such as perylenes,[8] cyanines,[9] porphyrins,[10–12] imidazoles,[13] and thermally activated delayed fluorescence (TADF) dyes[14,15] have been investigated as potential substitutes.[16] However, they have generally shown inferior performance compared to organo-metallic complexes in completed devices. The development of rare-metal-free LECs exhibiting stable and efficient luminance is consequently of high interest for achieving future lighting devices that are sustainable and economical.

As a step toward this objective, we report herein the detailed investigation of an overlooked class of imide-containing rylene, namely benzothioxanthene imide (BTI). Although this class of dye has been known since the late 70s, little work has been dedicated to fully understand and exploit their spectroscopic properties. Recently, our team demonstrated that selective chemical modifications can endow these chromophores with exceptional

K. K. Leong, H. J. Kim, J. Kim, Y. Auh, D. Kim, E. Kim
Department of Chemical and Biomolecular Engineering
Yonsei University
50 Yonsei-ro, Seodaemun-gu, Seoul 03722, South Korea
E-mail: eunkim@yonsei.ac.kr

The ORCID identification number(s) for the author(s) of this article can be found under https://doi.org/10.1002/adom.202401700

DOI: 10.1002/adom.202401700

K. Morice, P. Josse, D. Puchán Sánchez, P. Blanchard, C. Cabanetos
CNRS
MOLTECH-ANJOU
SFR MATRIX, Angers F-49000, France
E-mail: clement.cabanetos@cnrs.fr

C. Monnereau
ENS de Lyon
CNRS
LCH, UMR 5182
Lyon, cedex 07 F-69342, France
E-mail: cyrille.monnereau@ens-lyon.fr

C. Cabanetos, E. Kim
Building Blocks for FUture Electronics Laboratory (2BFUEL)
IRL2002
CNRS -Yonsei University
50 Yonsei-ro, Seodaemun-gu, Seoul 03722, South Korea

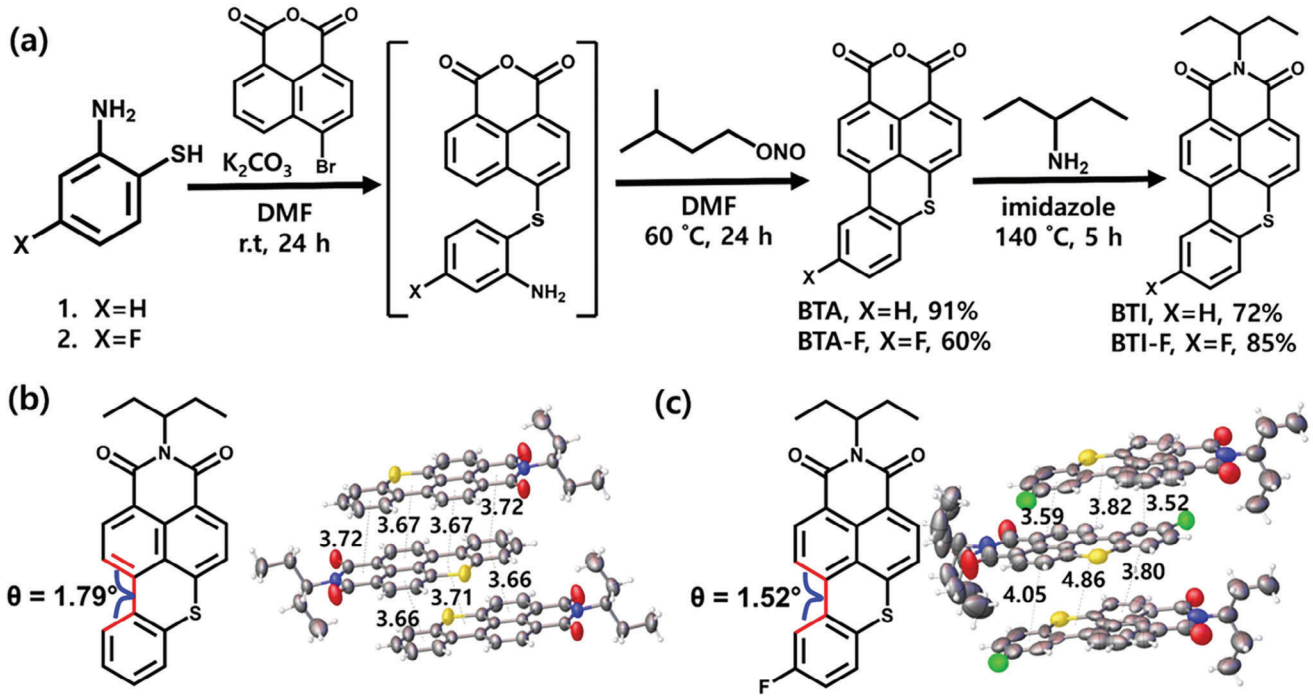

Figure 1. a) Synthesis scheme of BTI and BTI-F. b,c) Structures and single crystal XRD structure of dyes BTI (b) and BTI-F (c).

photophysical features.[17–19] These advancements can be leveraged in various advanced material applications, including photodynamic therapy,[20–22] photocatalysis,[23] and electroluminescent devices.[24] In the present work, owing to new site-selective derivitizations of their π-conjugated backbone, and careful integration into electroactive layers, optimization of the optical, electrochemical and self-assembly properties led to significant enhancements in their device performances. However, despite high luminescence in the solution state, these BTI derivatives molecules are highly prone to π–π stacking, resulting in the well-known aggregation caused quenching (ACQ) effect in the solid state. This constitutes a highly detrimental feature in view of their otherwise straightforward application in light-emitting electrochemical cells. Host materials were thus introduced into the active layer to mitigate those effects.

Although doping LEC active layers with host molecules is a well-known strategy, its purpose is generally to enhance the emission by promoting the energy transfer from host to guest through the suppression of exciton-polaron quenching. This approach requires a large overlap between the emission spectrum of energy donor (host) and the absorption spectrum of fluorescent emitter (guest) and suitable intermolecular distance between host and fluorescent guests. Additionally, hosts can also be useful as binders to improve the film processability and morphology.[25] Given that the performance of LECs with small molecules is highly dependent on interactions between fluorescent emitters (guests) in thin films, the design of multicomponent host-guest systems has emerged as a way to minimize exciton quenching in the active zone.[26–29] For instance, in 2017, Tang et al. introduced the strategy of using more than one host in the active layer to increase the conductivity of the *p*–*n* doping region and several multi-hosts examples were then reported.[30,31] In this approach, the *p*–*n* doped region must be balanced to avoid exciton-polaron quenching in the emission zone. This creates a trap-free region in the doped part of the device, which allows unhindered transport of both holes and electrons to the recombination zone. Inspired by these pioneering works, we therefore, introduced 4,4′-bis(N-carbazolyl)-1,1′-biphenyl (p-CBP) as a n-type host to interact with the alignment of the BTIs, in combination with p-type host polymers which act as surface binders to improve the film morphology. Once blended with host materials, BTI dyes were able to retain their high luminescence by suppressing their inherent ACQ effect, while at the same time balancing charge transport through the use of appropriate n-type and p-type multi-hosts. In particular the energy transfer from the host and reduction of resistance for carrier transport resulted in a high luminescence reaching values up to ca 3900 cd m^{-2}. These results thus highlight the great potential of this new class of metal-free dye for OLECs while opening doors to new design principles and advanced device engineering approaches.

2. Results and Discussion

2.1. Photophysical and Electrochemical Properties of BTI Dyes

Two different BTI dyes (**Figure 1a**; Figures S1 and S2, Supporting Information) were synthesized starting with 4-bromo-1,8-naphthalic anhydride, which engaged in a nucleophilic aromatic substitution reaction with either aminobenzenthiol **1** or **2** to generate intermediates **3** and **4**, respectively. The latter directly reacted with isoamyl nitrite to afford the anhydrides BTA and BTA-F in good yields. Imidization cyclization was then carried out in molten imidazole with pentan-3-amine to afford the target compounds, namely, the BTI and BTI-F. Herein, a fluorine atom was

introduced, for the first time on a BTI substrate, to promote intermolecular halogen interactions among the molecules. Structures were confirmed by X-ray diffractometry performed on single crystals which were successfully grown from the slow evaporation of toluene solutions (Figure 1b,c; Figure S3,S4, and Table S1, Supporting Information).[24,32] From these data, it appeared that both BTI dyes show planar structures across the π-conjugated network with a slight difference in dihedral angle (θ) in the bay position (**Table 1**), with a 2θ value of 1.79° for BTI and 1.52° for its fluorinated counterpart. Because of its structural similarity BTI and BTI-F, both crystallized in a similar triclinic structure and showed a typical head-to-tail packing. A shortest centroid-to-centroid distance of 3.66 Å was observed for BTI, while a reduced distance was measured for BTI-F (3.52 Å). Furthermore, both BTIs showed a variety of intermolecular interactions mainly originating from the π–π stacking of the planar network, such as H–H (54.4%), C–C (14.9%) and C–H (10.5%), as well as hydrogen bonds such as H–O (12.1%) and H–S (5.6%). The introduction of fluorine was found to i) increase the overall hydrogen bonding fraction to the proportions H–O (11.8%), H–F (11.2%) and H–S (4%) and ii) cause tighter packing compared to the BTI (supported by the shorter distance between two interacting C–C atoms). The shortest interacting distance of 3.48 Å for BTI was found to decreases to 3.04 Å for its fluorinated counterpart which appeared to stem from the two C_{38}–C_{38} atom interactions located diagonally to each other.

The ground state geometries in vacuum were also computed for both dyes using density functional theory with the B3LYP functional and the 6–31G (d, p) basis set.[33] The geometries of the BTI dyes calculated by DFT are in good agreement with the experimental SCXRD-resolved structure.

In parallel, the thermal properties of the BTI dyes were characterized using differential scanning calorimetry (**DSC**), thermogravimetric analysis (**TGA**) and differential thermal analysis (**DTA**) (Figure S5, Supporting Information). The melting point (T_m) of BTI-F in DSC was found to be higher than that of BTI (273 °C vs 235 °C respectively) which may originate from the additional H—F hydrogen bonds in BTI-F. The TGA results showed a similar trend since BTI started to decompose at 287 °C while a value of 301 °C was observed for BTI-F, highlighting its improved thermal stability. From the DTA data, both dyes showed a positive area under the graph which indicates an exothermic reaction upon combustion.

Regarding their optical properties, the absorbances of both derivatives were first examined at room temperature in chloroform (1×10^{-7} M). While both dyes showed a strong absorption band in the visible region, assigned to $\pi \rightarrow \pi^*$ transitions, BTI-F showed a slightly red-shifted absorption (462 nm) compared to that of BTI (458 nm). From the photoluminescence point of view, BTI dyes show a strong fluorescence in the green region and the emission of BTI-F also appeared slightly red-shifted compared to that of BTI (508 vs 501 nm, respectively), thus highlighting the impact of the fluorine substitution on the optoelectronic properties (**Figure 2a**).[34,35]

Apart from that, these dyes showed significant positive solvatochromism behavior, evidenced by a notable red-shift in emission as the solvent polarity increased. Both BTI and BTI-F exhibit a structured emission with distinct vibronic features while higher photoluminescence in non-polar solvents, such as hexane, was recorded for BTI-F than BTI (Figure 2b). However, in polar solvents, the emission of BTI-F becomes weaker and more red-shifted than that of its non-halogenated counterpart (BTI), which may be attributed to a slight increase in the intramolecular charge transfer character of the halogenated fluorophore, which is known to reinforce vibronic nonradiative processes (a positive solvatokinetic effect in more polar solvents).[36] For example, the luminescence of BTI-F was mildly quenched and red-shifted to 514 nm in chloroform, compared to BTI at 503.5 nm. A similar trend was observed in THF, where BTI-F showed lower emission at 507.5 nm, compared to BTI at 502 nm.

Figure 2c shows the PL peak intensities and wavelengths of the two dyes in THF/water mixtures at different ratios. As the water fraction increased, forcing the aggregation of the dyes, luminescence of BTI-F was found to be significantly reduced, and, in fine, almost entirely quenched while shifting to the red (514 nm). This behavior confirmed that both dyes underwent ACQ in THF/water mixture which reveals the detrimental effects of ACQ on PL efficiency in the solid state and ultimately in the functional device.

Cyclic voltammetry (**CV**) was carried out to gather information about the highest occupied molecular orbital (**HOMO**) and lowest unoccupied molecular orbital (**LUMO**) levels (Figure 2d). While BTI showed a clear reversible oxidation peak at +0.93 V, an irreversible oxidation peak at +0.90 V was recorded for BTI-F. This slight decrease can be attributed to the inductive electron withdrawing effect of the fluorine substitution, which also seems to impact stability of the oxidized species. Regarding the reduction, while the BTI showed a reversible reduction peak at −1.74 V, BTI-F showed a quasi-reversible reduction here again shifted to a lower potential with a peak at −1.07 V. The HOMO and LUMO energies of BTI-F, estimated using the Nernst equation from these CV data, were found to be more positively shifted compared to that of BTI, likely because of the mesomeric effect induced by the fluorine substituent. As a result, a significant decrease in bandgap was calculated for BTI-F with $E_g = 2.09$ V compared to BTI, characterized by an E_g of 2.30 V. The decrease in the bandgap energy induced by the fluorine substitution was further supported by density functional theory (**DFT**) calculations and is also in line with the red shift in the UV and PL spectra as discussed above. Note that both BTI and BTI-F show similar computed HOMO and LUMO distributions (**Table 2**; Figure S6,

Table 1. Single crystal parameter summary.

Dye	$\theta_{Exp.}$ [°]	θ_{DFT} [°]	Plane distance [Å]	Shortest π–π interaction [Å]	Shortest C-C interaction [Å]	Hydrogen bond [%]	α	β	γ	Crystal type
BTI-F	1.52	0.0022	10.47	3.521	3.04	27	101.60	90.28	111.32	triclinic
BTI	1.79	0.0022	10.44	3.655	3.48	18.1	105.44	92.76	104.12	triclinic

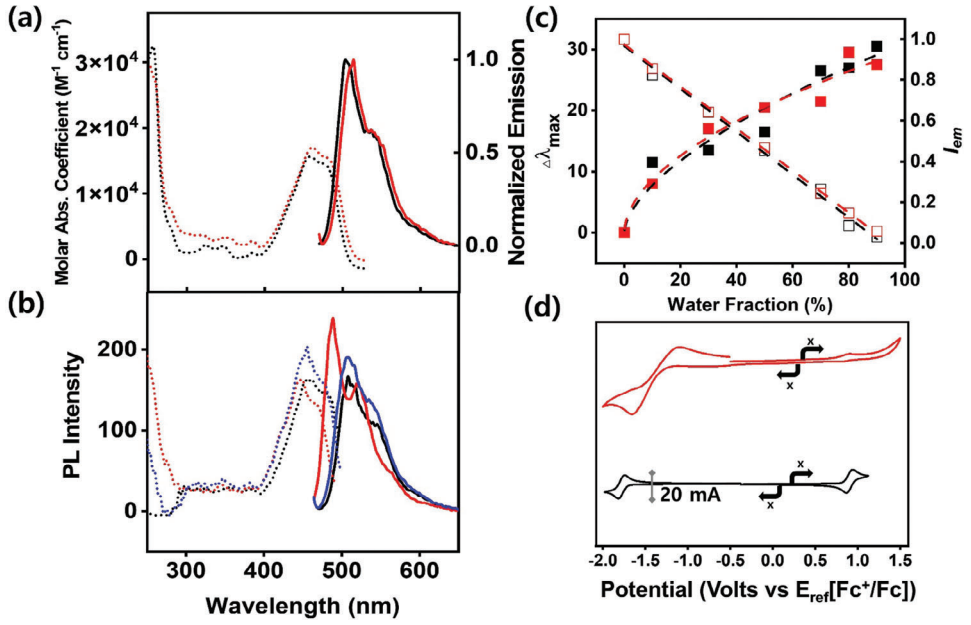

Figure 2. a) Absorbance (dotted) and photoluminescence spectra (solid) of dyes (10^{-7} M in chloroform): BTI (black), BTI-F (red). b) Solvatochromism of BTI-F in chlorobenzene (black), hexane (red) tetrahydrofuran (blue); excitation spectra (dotted) and photoluminescence spectra (solid). c) The PL peak intensity change (I_{em}, empty) and the corresponding wavelength shift ($\Delta\lambda_{max}$, solid) of BTI (black) and BTI-F (red) in THF/water mixtures with different water fractions. d) Cyclic voltammograms of BTI (black) and BTI-F (red) in degassed CH_2Cl_2 solutions (1 mM) using tetrabutylammonium perchlorate as the electrolyte (0.1 M), platinum disk electrode as the working electrode, platinum wire as the counter electrode, Ag/Ag^+ as the reference electrode and a scan rate of 100 mV s^{-1}.

Supporting Information).

2.2. LEC Properties of BTI Dyes Without Host and with Single Host

The LEC properties of the BTI dyes were first explored using the simplest device structure comprising active layers without any host (**Figure 3a**). In this case, the BTI dyes were mixed with tetrahexylammonium tetrafluoroborate (**THAB**) with a weight ratio of 4.7:5.3 before being dissolved and spin-coated on top of 35 nm thick poly(3,4-ethylenedioxythiophene):poly(styrenesulfonate) (**PEDOT:PSS**) layers which were pre-coated on indium-tin oxide (**ITO**) anodes. A 100 nm thick aluminum back cathode was then deposited by thermal evaporation to complete the device. This system is labelled dye/T, where dye is either BTI or BTI-F and T, the THAB electrolyte. BTI-F/T and BTI/T devices were turned on using the direct current IVL method in which the voltage was increased at a rate of 0.1 V s^{-1}. This method produced a faint orange emission visible to the naked eye from both devices, though the luminance did not exceed 1 cd m^{-2}, as measured by a Konica Minolta CS-2000 spectroradiometer (Figure S7, Supporting Information). Initially, electroluminescence (**EL**) measurements of the host-free BTI-F and BTI LECs were intended to reveal effect of the fluorine substitution on color and luminance efficiency. However, these attempts remained unsuccessful due to the extremely weak light intensity. This issue was likely caused by the severe ACQ effect already observed in our prior spectroscopic investigations, indicating that the THAB electrolyte alone does not adequately prevent the packing and consequent ACQ of the BTI based dyes. No fluorescence was observed under exposure of the films to 256 nm and 365 nm UV light, and only faint emission was detected through PL spectroscopy. Conversely, solid state UV spectroscopy revealed that BTI-F and BTI both showed a weak absorption in the visible, with characteristic maxima at 471 and 466 nm, respectively. The significant red-shift (*ca* 10 nm in both cases) compared to similar data in solution may be attributed to pronounced π–π interactions in the solid state. Due to the strong aggregation-caused quenching (ACQ) effect, attempts to measure photoluminescence resulted in low, poorly defined emissions, making it impossible to accurately determine the emission maxima.

Table 2. Energy levels of BTI dyes.

Dyes	Electrochemical		DFT calculation	
	HOMO	LUMO	HOMO	LUMO
BTI-F	−5.53	−3.49	−5.52	−3.14
BTI	−5.63	−3.10	−5.42	−2.95

In order to mitigate the ACQ effect in solid state and enhance the overall device efficiency, hosts were thus introduced in the active layer matrix. Blended with the BTI dyes, hosts were used to intercalate between the BTI dye molecules and induce sufficient steric repulsion to prevent close contact of the planar conjugated networks in the BTI fluorophores by disrupting the regular ordering of the structure.[37]

In this study, three different hosts were investigated for introduction within the BTI based LEC since, based on

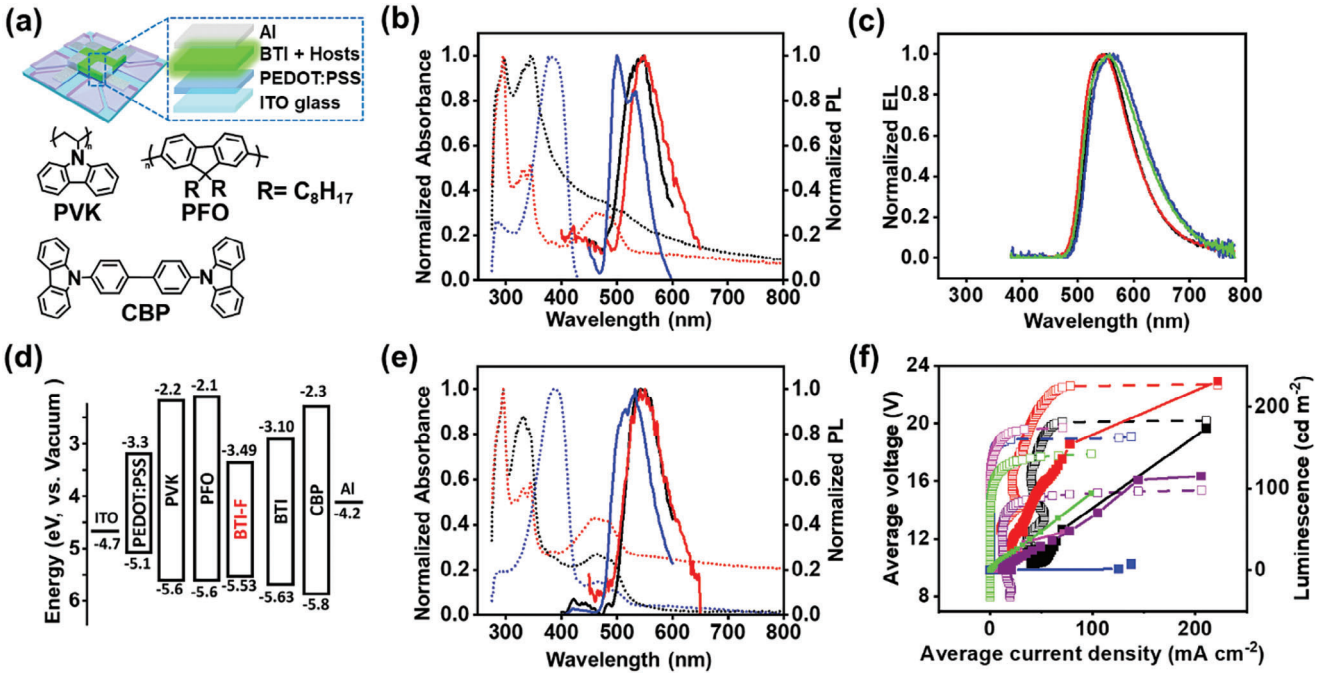

Figure 3. a) Schematic diagram of the LEC devices and chemical structure of the hosts. b) Normalized absorption (dotted line) and photoluminescence (solid line) of BTI based LEC films: BTI-F/CT (black), BTI-F/VT (red), BTI-F/FT (blue), excited at their absorption maximum. c) EL spectra of the single host LEC device with BTI-F/CT (black), BTI/CT (red), BTI-F/VT (blue), and BTI/VT (green). d) Schematic energy level diagram of the dyes and host. e) Normalized absorption (dotted line) and photoluminescence (solid line) of BTI-F based LEC films BTI/CT (black), BTI/VT (red), BTI/FT (blue), excited at their absorption maximum of corresponding film. f) The voltage (empty square) and luminescence (filled square) variations under increasing applied average current density for BTI/CT (black), BTI-F/CT (red), BTI/VT (purple), BTI-F/VT (green), BTI/FT (magenta) and BTI-F/FT (blue).

previous reports,[38] suggesting that these hosts could mitigate the ACQ effect by preventing face-to-face stacking of planar co-mixed structures. Two p-type polymeric hosts, consisting of poly(9-vinylcarbazole) (**PVK**) and poly(9,9-di-n-octylfluorenyl-2,7-diyl) (**PFO**), were selected based on their energy levels and doping features (Figure 3d). Alternatively, 4,4′-bis(N-carbazolyl)-1,1′-biphenyl (**p-CBP**) was selected as a n-type host to fine tune the p-doping effect. From this point on, all of the devices discussed will refer to host-guest type LECs, in which the BTI fluorophores are embedded in one of the hosts mentioned above, abbreviated by a characteristic initial of host (i.e., C for p-CBP, V for PVK, F for PFO).

To examine the effect of the host in the LEC devices, the mutual solubility of hosts and guests was first investigated to understand phase separation and ensure optimal film homogeneity, which is crucial for smooth and balanced charge carrier transport throughout the device. Three different solvents – chlorobenzene, cyclohexanone and o-xylene- were investigated in this context. It is noteworthy that o-xylene is a halogen-free, relatively green solvent which is compatible with industrial printing techniques and has already been used for the fabrication of other BTI derivatives in OLED devices.[31] However, using BTI-F/CT as the reference system, LEC devices processed with chlorobenzene exhibited the highest luminescence (241.9 cd m^{-2}), significantly outperforming devices processed with cyclohexanone (43.9 cd m^{-2}) and o-xylene (3.1 cd m^{-2}) (Figure S8a, Supporting Information).

In order to rationalize the difference in luminescence efficiency, films were analyzed by optical microscopy (Figure S8b-d, Supporting Information). Indeed, the morphology of the films processed from chlorobenzene showed relatively small aggregates, which may originate either from minor phase segregations between p-CBP and BTI-F or by the presence of microcrystalline domains of the host-guest mixtures. In contrast, films obtained from cyclohexanone showed large aggregates which may have arisen from the distinct de-wetting behavior of p-CBP and BTI-F, leading to significant phase separation. The lowest luminescence was observed with o-xylene, likely due to the poor solubility of p-CBP in this solvent. Consequently, chlorobenzene was selected as the solvent for all of the subsequent device fabrications in this study.

The PL spectra in the presence of hosts indicate energy transfer from the host to the guest, as evident in the emission spectra, which perfectly matches the fluorescence signature of the BTI derivatives (Figure 3b,e). Prior to assessing the effect of the host on the performance of the LEC, the optimal host:dye:THAB ratio was determined. While maintaining the total weight of host, LEC performance were evaluated with different weight percentages of BTI dyes (36%, 18%, 9%). The best results were achieved at an 18% wt. ratio, resulting in a luminescence of 241.9 cd m^{-2} and a peak current efficiency of 187.8 mA cm^{-2} for the p-CBP based devices (Figure S9a, Supporting Information). Further increase in the amounts of guests resulted in a drop in maximum luminescence to 161.9 cd m^{-2}. This optimal performance likely results from a balance between the initial increase in luminescence upon increasing BTI concentration, and the onset of nucleation of π-stacked aggregates at higher

BTI loading, which exacerbates ACQ effect. This conclusion is also supported by the red-shift in the electroluminescence (**EL**) observed as the guest weight increased from 9% to 36% (Figure S9b,c, Supporting Information), mirroring the shift seen upon increasing the water fraction in the nanoprecipitation experiments (Figure S10, Supporting Information). Additionally, we postulate that this aggregate formation may hinder the mobility of electrolyte ions and lead to exciton quenching, explaining the reduction of the maximum current density to 112.1 mA cm^{-2}. Consequently, the guest weight was fixed at 18% and this ratio was used in all the subsequent systems presented in this work in order to focus on the effect of the host on device performance.

Overall, BTI-F/CT (241.9 cd m^{-2}) showed higher luminescence than BTI/CT (173.4 cd m^{-2}) which may arise from improved interactions of the fluorinated dye with p-CBP. These interactions help reduce aggregate formation, thereby preventing ACQ (Figure 3f).

To further investigate this hypothesis and rationalize the beneficial influence of fluorination of the BTI on the device properties, interactions between the guest and host were simulated using density functional theory (**DFT**) model using the Gaussian 09 program (Figure S11a,b and Table S2, Supporting Information). These calculations reveal that BTI-F shows a stronger interaction with p-CBP molecule stemming from the presence of the fluorine atom, leading to tighter packing of the host and guest molecules: specifically, a shorter intermolecular distance of 3.26 Å was estimated for BTI-F compared to *ca* 3.47 Å for BTI. Hence, the addition of a fluorine atom in BTI clearly resulted in a more favorable interaction with p-CBP which may i) reduce homomolecular stacking of the BTI derivatives and more efficiently limit ACQ and ii) favor the host-guest energy transfer process through a FRET mechanism. Interestingly, DFT calculations reveal that BTI-F showed a more tilted structure with a dihedral angle of 13.98° compared to ca 10.96° for the BTI. This feature might also contribute to limiting the ACQ effect (reducing π- π stacking via molecular distortion), thereby improving luminescence efficiency.

Both BTI-F/CT and BTI/CT based devices emitted yellowish green electroluminescence with maxima at 550 and 545 nm (Figure 3c). The BTI-F/CT showed a FWHM of 91 nm, slightly narrower than that of its non-fluorinated counterpart (99 nm for BTI/CT). This is consistent with restricted conformational mobility expected from a stronger, tighter packing with p-CBP and decreased aggregation-induced polymorphism.

In contrast, when using polymeric p-type hosts such as PVK and PFO, the opposite influence of the fluorine atom on the luminescence was observed. BTI/VT and BTI/FT displayed higher luminescence values of 156.4 and 85.7 cd m^{-2}, respectively, compared to the fluorinated BTI-F-based devices (93.8 and 7.3 cd m^{-2}, respectively). For the latter, the significant drop in luminescence efficiency observed upon replacement of p-CBP by polymer hosts indicates that CBP plays two crucial roles: first, its close interaction with BTI dyes (particularly BTI-F) helps disrupt aggregation, preventing ACQ; second, p-CBP serves as both n- and p-type dopant, as indicated by its voltammogram and energy levels, contributing to in situ charge balance, as previously reported.[39] The comparatively lower luminescence in the VT and FT systems may be attributed to unbalanced doping, which shifts the recombination zones away from the center of the active layer. This displacement leads to exciton-polaron interactions, reducing the amount of harvestable triplet energy.

From an energy transfer perspective, the photoluminescence of PFO shows good overlap with the absorbance of the guest molecules, which should favor higher FRET efficiency. However, once embedded in LECs, low luminescence was observed, likely due to the long alkyl chains of the PFO that hinder close contact with the emitting dyes. This structural limitation, which presumably reduces FRET efficiency, is illustrated by the electroluminescence (EL) peaks observed at 499 nm for BTI-F/FT and 530 nm for BTI/FT. In both cases, the EL spectra feature a combination of PFO centered emission (peaking at 438.5 nm) and BTI centered emission (peaking at 557 nm) indicating incomplete energy transfer from the former to the latter (Figure S9d, Supporting Information). In contrast, complete energy transfer was observed with the less sterically hindered PVK, where an EL maximum was observed at 557 nm for both BTI dyes. The FWHM values varied significantly depending on the host material. While PFO exhibited a FWHM of 70 nm, p-CBP and PVK showed broader peaks at 99 and 115 nm, respectively. Again, this broadening can be attributed to increased conformational disorder or polymorphism across the series. These results suggest that greater segregation of BTI molecules occurs in PFO, where the long alkyl chains may act as a shield between BTI moieties, whereas p-CBP and PVK display poorer dispersion, with PVK showing the greatest degree of aggregation.

The effects of the PFO can also be directly observed from the normalized UV absorption spectra (Figure 3b,e). LEC films based on the FT host indeed showed a major absorption centered around 390 nm, which corresponds to the absorbance of thost. In other words, when PFO is embedded as the sole host, it is responsible for the majority of the emission. This observation is further supported by the photoluminescence spectra in which the main emission also comes from the PFO.

The above PL studies revealed that the combination of BTI and PFO did not effectively prevent dye aggregation quenching (ACQ), primarily due to a lack of host-guest interactions, as evidenced by the low PL intensity from the guest. Conversely, the use of the fluorinated dye, which mitigates self-aggregation while favoring better interaction with the host, resulted in enhanced PL intensity.

Conversely, when CT was used as a host, the BTI blend showed an obvious π–π stacking peak around 450 nm which was absent in BTI-F/CT. This disappearance indicates an effective suppression of the ACQ effect. DFT calculations were performed on the present system to rationalize this feature (Figure S11a,b, Supporting Information). Characterized by a tilted structure in its free form,[40] p-CBP adopts a more planar conformation once blended with the guest, due to strong π–π interactions with the π-conjugated backbone of the BTI (Table S2, Supporting Information). The plane angle between the carbazole and the diphenyl in p-CBP was found to be smaller when mixed with BTI-F (52.6°) than with BTI (53.8°), reflecting enhanced π–π interactions with the fluorinated dye. As a result, the π–π interactions in p-CBP-BTI blends contributed in limiting the strong BTI-BTI intermolecular π–π stacking, therefore reducing the ACQ effect.[41,42]

Next, FT-IR experiments were carried out to investigate π–π interactions between the host and guest components in the active layer. Significant changes were observed in the aromatic C–H

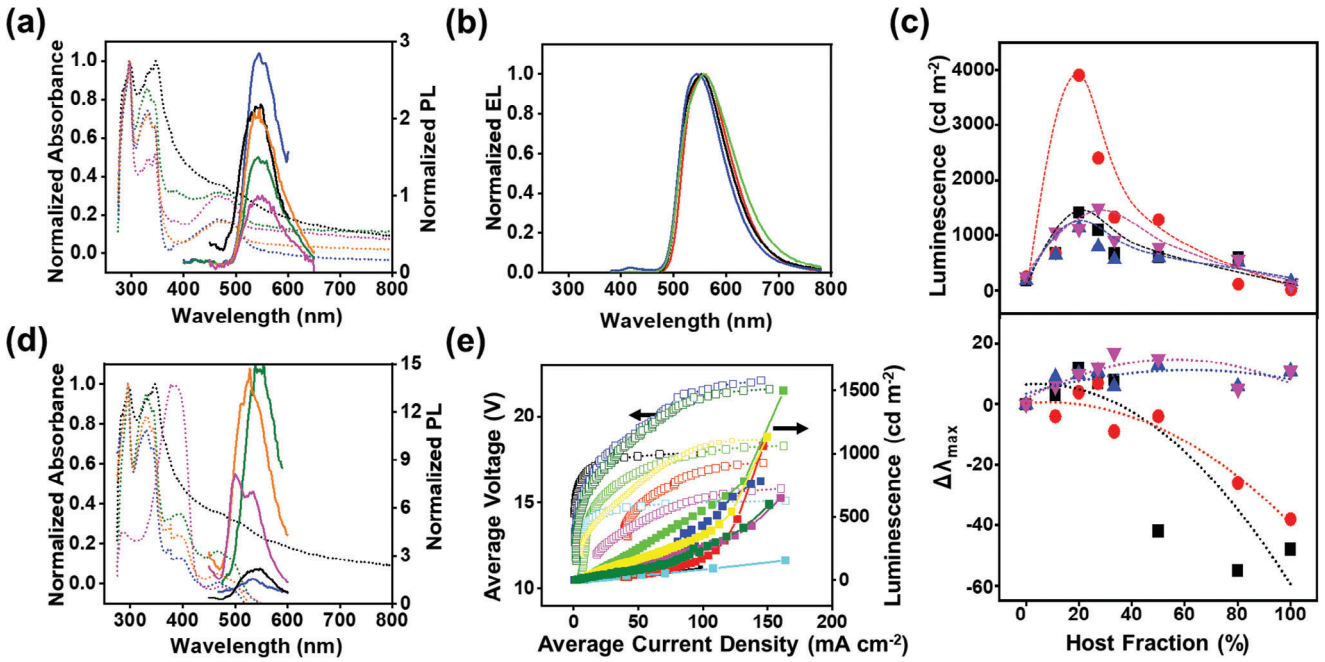

Figure 4. a) Normalized absorbance (dotted line) and photoluminescence (solid line) of BTI-F based dual host LEC films BTI-F/CT (black), BTI-F/CVT (C:V = 8:1, green), BTI-F/CVT (C:V 8:2, blue), BTI-F/CVT (C:V = 8:4, orange), BTI-F/VT (magenta), excited at their absorption maximum of corresponding films. b) EL spectra of the dual host LEC device with BTI dyes: BTI/CVT (C:V = 8:2, black), BTI-F/CVT (red), BTI/CFT (green), BTI-F/CFT (blue). c) Relation between the host fraction and maximum intensity (top) and wavelength change (bottom) for BTI dyes in the CVT and CFT devices: BTI/CVT (blue), BTI-F/CFT (red), BTI/CFT (black), and BTI-F/CVT (magenta). d) Normalized absorption (dotted line) and photoluminescence (solid line) of BTI-F based dual host LEC films BTI-F/CT (black), BTI-F/CFT (C:F = 8:1, green), BTI-F/CFT (C:F = 8:2, blue), BTI-F/CFT (C:F = 8:4, orange), BTI-F/FT (magenta), excited at the absorption maxima of corresponding films. e) Voltage (empty square) and efficiency (filled square) variations under increasing applied average current density for the multi host LEC devices: BTI-F/VT (black), BTI-F/CVT (C:V = 8:1, red), BTI-F/CVT (C:V = 8:3, green), BTI-F/CVT (C:V = 1:1, blue), BTI/VT (cyan), BTI/CVT (C:V = 8:1, magenta), BTI/CVT (C:V = 8:2, yellow), BTI/CVT (C:V = 1:1, olive).

stretching region of the IR spectrum of BTI-F (guest) doped in p-CBP (host). The peaks at 718 cm^{-1} (C–H stretching of carbazole out of plane) and 827, 1306 cm^{-1} (C–H stretching of biphenyl) were found to shift as the guest concentration increased. A maximum shift was observed at an 18% guest concentration, which was considered to be the optimal doping level (Figure S11d-f, Supporting Information).[43]

2.3. LEC Properties of BTI Dyes with Dual Host

Since high luminescence was not achieved in single host devices, due to unbalanced doping in the active layer, dual host systems were explored. These systems combined a polymeric p-type and a n-type host with THAB electrolyte. Specifically, BTI derivatives, p-CBP, PFO, and THAB were blended in a 15.9:53.0:13.1:17.8 ratio and dissolved in chlorobenzene. The EL emission was significantly enhanced, with luminescence measured at ≈3900 cd m^{-2} with a maximum at 549 nm for BTI-F/CFT and 1407.9 cd m^{-2} at 557 nm for BTI/CFT (Figure S12a, Supporting Information). These results represent a 17-fold increase in luminescence for BTI and an impressive 650-fold increase for the fluorinated BTI when shifting from single to dual host systems.

As shown in Table S3 (Supporting Information), the maximum luminescence of the BTI-F device at the optimized host composition is among the highest reported to date for LECs based on heavy-atom-free organic small molecules.

The dual hosts approach was extended to include PVK, using the same weight ratios as in the FT systems. However, in this case, the luminescence of BTI-F/CVT was adversely impacted, decreasing to *ca* 34.0 cd m^{-2}. This reduction is likely due to overdoping issues with the THAB electrolyte in the film. While increasing THAB can enhance average current density and peak luminescence, excessive amounts can cause excessive current and an unbalanced flow of charge carriers, ultimately reducing electroluminescence efficiency. To test this hypothesis, the quantity of the THAB in BTI-F/CVT was reduced while keeping the proportions of all the other components constant, resulting in a composition of BTI:p-CBP:PVK:THAB = 18.2:60.7:14.2:6.7 (**6%T**) and 18.9:63.1:14.8:3 (**3%T**). As expected, the 6%**T** ratio showed enhanced luminescence, reaching values up to 761.4 cd m^{-2} while the 3%**T** achieved up to 1113.5 cd m^{-2} (Figure S12b, Supporting Information), thus confirming our initial hypothesis. Both devices showed well-resolved emission peaking at 557 nm, with no trace of residual host emission regardless of the THAB content, indicating complete energy transfer from the host to the guest (**Figure** 4b). As a result, luminescence of the BTI-F/CVT was increased by a factor of 5 compared to BTI-F/CT and nearly a factor of 12 compared to BTI-F/VT.

The dual host systems approach for BTI derivatives was then extended to CFT and the CVT hosts. In that case, BTI/CFT showed lower luminescence efficiency than BTI-F/CFT with peak luminescence at ≈1407.9 cd m^{-2}, which is about half of that observed for BTI-F/CFT. This observation aligns with the previously

observed weaker interaction between p-CBP and BTI, which may favor partial self-aggregation of the latter. This limited interaction increases the distance between the host and the guest, which is detrimental to energy transfer. Both BTI/CVT and BTI-F/CVT showed similar luminescence, with maximum values of ≈1134.5 cd m^{-2} for BTI/CVT and 1113.5 cd m^{-2} for BTI-F/CVT, associated with an emission band centered at 556 nm (Figure 4e). Lower luminescence of both CVT based systems compared to their CFT counterparts further supports our hypothesis that the long alkyl chains help prevent BTI self-aggregation, thereby mitigating the ACQ effect.

Based on these encouraging results, different combinations and ratios of *p–n* dopants were then evaluated for the CFT and the CVT dual host systems to achieve optimal charge balance. To isolate the effect of the host materials, the weights of the guest and the electrolyte were fixed while varying the amount of p-CBP, PVK and PFO (Figure 4c). In the case of BTI-F/CFT, the luminescence gradually increased from 241.9 to 3906.7 cd m^{-2} as the fraction of PFO was increased from 0.0% to 20.0% (C:F = 8:2). However, further increase of the PFO fraction resulted in the decrease of the luminescence from 2402.1 cd m^{-2} at 27.3% (C:F = 8:3) to 1328.0 cd m^{-2} at 33.3% (C:F = 8:4) down to 110.2 cd m^{-2} at 80% (C:F = 2:8). Microscopic analysis revealed that increasing the PFO content resulted in degraded film morphology with phase-segregated domains. Thus, while a small amount of polymer host (<35%) can contribute to achieving uniform films and balancing electronic transport, excessive PFO appears to negatively affect film morphology, leading to reduced luminescence. Similarly, the BTI/CFT system also reached a peak luminescence value of 1407.9 cd m^{-2} at a 20.0% of PFO (C:F = 8:2) of PFO, while consistently showing lower luminescence efficiency compared to BTI-F/CFT across all PFO ratios. The evolution of the absorbance and photoluminescence spectra of the dual host systems with varying PFO/PVK to CBP ratios (Figure 4a,d) show a similar trend as the EL data.

In a similar fashion as for the CFT doped active layers, an initial increase in luminescence efficiency was initially observed upon increasing PVK concentration in the CVT active layer, before dropping at higher loading. In the present case, BTI-F/CVT showed a peak luminescence of 1494.5 cd m^{-2} with 27.3% (C:V = 8:3), while BTI/CVT peaked at 1134 cd m^{-2} at 20.0% PVK (C:V = 8:2).

As the dual host LECs achieved high luminescence, these systems were evaluated using the pulsed current luminescence (**PCL**) method in an attempt to better form electrical double layers (EDL). We thus aimed to i) reduce the turn-on voltage, ii) improve the speed of the turn-on time (usually resulting in higher efficiencies) and iii) increase luminescence.[44,45] To investigate this, a current pulsed at 235 Hz and 50% duty cycle was applied, turning on the device for 1 s before switching it off for 29 s (Figure S13, Supporting Information). In the BTI-F/CFT dual host system the turn-on voltage decreased from 14.6 V to 11.9 V (IVL vs PCL method), while the luminescence remained ≈2380 cd m^{-2}. Notably, the voltage did not increase linearly with the applied current (Figure S13d,e, Supporting Information). These results suggest that the long alkyl chains of PFO may impede charge flow, leading to sub-optimal operating conditions.

With a reduced turn-on voltage (6.2 V vs 11.2 V), the stability of BTI-F/CVT was slightly improved compared to that of BTI-F/CFT (**Figure** 5d). In long-term stability tests, the latter indeed reached its maximum within 100 s at a constant bias operation with a half-life ($t_{1/2}$) of 200 s, whereas BTI-F/CVT achieved a $t_{1/2}$ of ≈260 s (Figure 5e). Despite both systems demonstrating fast *p–n* junction formation and very short turn-on times, their relatively low stability constitutes a limiting factor for practical applications. This instability may be due to an unbalanced charge carrier density, indicating that the optimal combination of host and guest has not yet been fully realized. In the 3-s on/off switchability test, BTI-F/CVT exhibited a noticeable increase in luminescence throughout the experiment. This effect is likely related to differences in the doping and de-doping rates, leading to the growth of the doped region between each cycle. After reaching the maximum luminescence of 440.3 cd m^{-2} driven by a pulsed current of 9 mA, the luminescence started to decrease slowly after 19 cycles. From cycle 20 to cycle 83 (after 500 s), the device's luminescence eventually stabilized at 114.1 cd m^{-2}, which remained easily visible to the naked eye (Figure S14a,b, Supporting Information).

2.4. Triple Hosts and Effect of the Host on the Performance

In an ultimate effort to address the aforementioned limitations and achieve a better balance of charge carriers for improved luminescence and stability, a new system was designed using a combination of three hosts: p-CBP, PVK, and PFO. The weight ratios of these hosts were similar to those used in the dual host systems. Specifically, the weight of the polymeric hosts was divided into two equal parts, with the total weight of the polymeric components maintained at less than 20% (BTI:p-CBP:PVK:PFO:THAB = 18.9:63.1:7.4:7.4:3). This proportion was chosen because it was shown to be optimal for achieving the highest luminescence in the dual systems.

The BTI-F/CVFT system was prepared as described and tested using the IVL method (Figure S15a, Supporting Information). It showed similar luminescence compared to its CVT counterpart (1493.7 cd m^{-2}). The EL spectra showed exclusive emission from the BTI-F guest, indicating complete energy transfer from PFO and PVK to the guest, a key factor for optimized performance (Figure 5c). The IVL sweep revealed a turn-on voltage of 8.2 V which corresponds to a 2.9 V decrease relative to CVT, and 6.4 V from the CFT blends. Moreover, these triple host devices turned on at a very low average current density of 1.0 mA cm^{-2}, significantly lower than the 10.7 mA cm^{-2} for CFT and 6.8 mA cm^{-2} for CVT (Figure 5d).

In the long-term pulse stability test (Figure 5e), BTI-F/CVFT devices showed an exceptional long $t_{1/2}$ of 3258 s (54.3 min). This value is significantly higher compared to BTI-F/CVT (12-fold increase) and BTI-F/FCT (16-fold increase), likely due to the enhanced charge carrier balance in the BTI-F/CVFT system. In the switchability test, the BTI-F/CVFT showed a good stability over 500 s, completing 83 on/off cycles, driven at a low pulsed current of 5.25 mA. The device reached its maximum luminescence of 215.0 cd m^{-2} in *ca* 150 s and remained stable after that. However, a small but significant decrease (≈ 20 cd m^{-2}) was observed after 300 s, probably caused by the joule effect (Figure 5f).

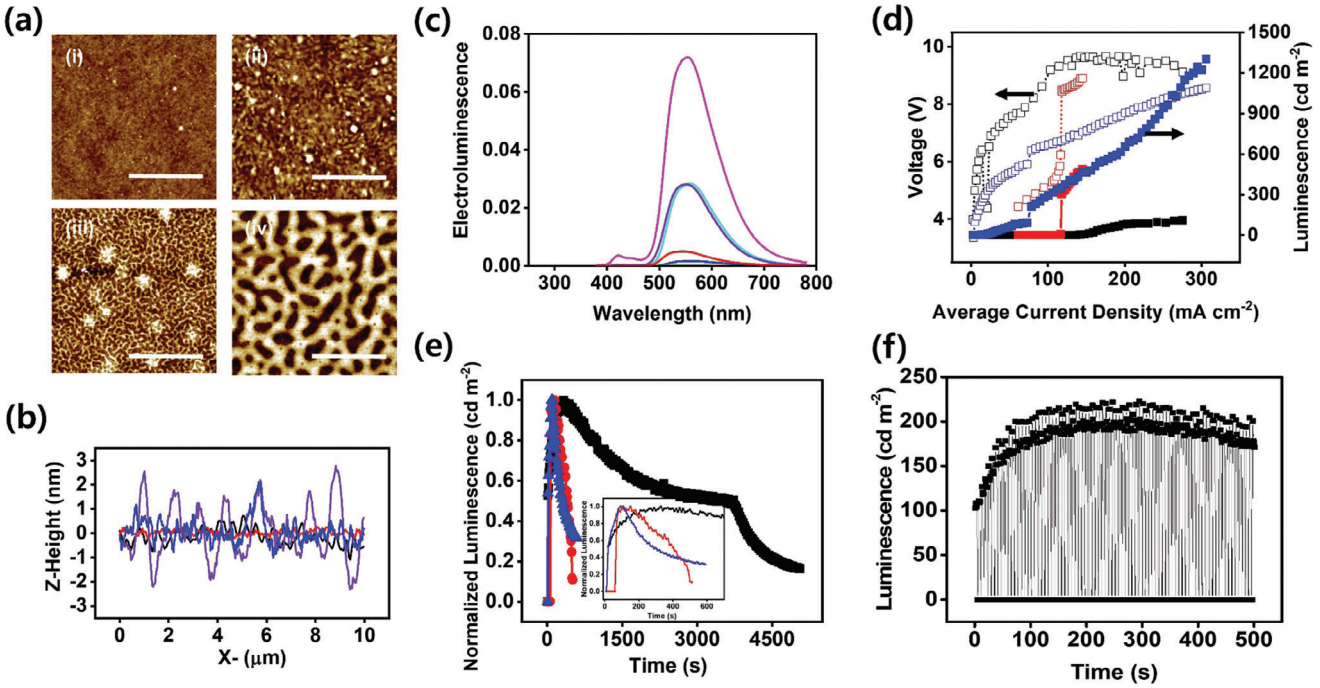

Figure 5. a) AFM images of the emitting films for LEC devices; i) BTI-F/CVT, ii) BTI-F/CT, iii) BTI-F/CFT, iv) BTI-F/CVFT (scale bar = 5 um). b) Height profile analysis on the film surface of i (red), ii (black), iii (blue), and iv (purple). c) EL spectra of the multi host LEC device with BTI-F: BTI-F/T (black), BTI-F/CT (red), BTI-F/VT (blue), BTI-F/FT (green), BTI-F/CVT (cyan), BTI-F/CFT (magenta) and BTI-F/CVFT (purple). d) Voltage (empty squares) and luminescence (filled squares) under increasing applied average current density for the BTI-F/multi host LEC devices; BTI-F/CT (black), BTI-F/CVT (red) and BTI-F/CFVT (blue) under pulsed current mode. e) Normalized luminescence changes over long term pulsed current testing for BTI-F/CVFT (black), BTI-F/CVT (red), and BTI-F/CFT (blue) devices. Inset: Normalized luminescence changes of each device over 600 sec. f) Stability of the BTI-F/CVFT devices upon 41 cycles of turn-on (≈3 s) and turn-off (≈3 s).

Following these tests, the device was continuously powered to evaluate its long-term stability under extended pulsed current application. Despite a decrease in brightness, the device maintained its output over 100 cd m^{-2} for an additional 500 s, resulting in a total runtime of 1000 s, which constitutes an exceptional stability for such a device (Figure S14c, Supporting Information). Under similar conditions, the BTI/CVFT device also exhibited good stability over 500 s. Its luminescence initially increased steadily, reaching a maximum of 300.8 cd m^{-2} after ≈200 s. However, it subsequently declined to ≈230.6 cd m^{-2} after an additional 500 s. When the device was subjected to continuous long-term pulsed current, a more rapid degradation occurred. The luminescence dropped below 101.6 cd m^{-2} after only 185 s, indicating faster performance deterioration compared to the BTI-F/CVFT device (Figure S14d, Supporting Information).

When tested under pulsed current, BTI-F/CVFT exhibited the lowest turn-on voltage with a value of 4.4 V. This low voltage can be attributed to balanced charge doping, as discussed earlier (Figure 5d). The BTI/CVFT system was also evaluated using the IVL method, where the luminescence decreased to 712.2 cd m^{-2}. This was accompanied by an emission centered at 544 nm which appears blue-shifted compared to that of BTI-F/CVFT. This likely relates to improved host-guest interactions as demonstrated by HR-XRD measurements performed on active layers (prepared in the exact same way as the LECs) spin-coated on silicon wafers (Figure S16, Supporting Information). The XRD spectra of BTI-F/T exhibit a distinct peak at $2\theta = 7.64°$, which corresponds to an interplanar distance of 11.6 Å. This value corresponds to the vertical distance measured from the nitrogen of the imide group to the opposite carbon on the lower benzene ring of BTI-F in the single crystal data, which also reveal that the presence of the ionic liquid does not disrupt the ordered alignment of BTI-F crystals. Conversely, introduction of p-CBP significantly suppresses the π–π stacking, leading to a fully amorphous XRD pattern, which correlates well with the high luminescence observed in the LEC devices. For the single-host system, intense XRD peaks were noted at $2\theta = 6.62°$ and 6.68°, corresponding to interplanar distances of 13.4 and 13.2 Å for VT and FT, respectively. Without a guest, the high intensity of the XRD patterns may originate from the crystallinity of the highly aligned PVK and PFO polymers. This phenomenon is known and reported in the literature for highly crystalline polymer structures.[46] The disappearance of the BTI-F peak at 7.64° after embedding in the polymer matrix indicates that the ACQ effect is effectively suppressed in the single host polymer. After the incorporation of p-CBP in the single host matrix, XRD patterns had a fully amorphous shape, indicating homogeneous films, without significant segregation or phase separation. Furthermore, the absence of any prominent peaks in the XRD spectra of the LEC films confirmed that guest molecule aggregation was completely suppressed in both the double- and triple-host systems.

The mechanisms behind the high luminescence characteristics of the multi-host system were investigated in further detail. From the perspective of energy transfer, the energy matching of

the host and the guest was evaluated using the Förster resonance energy transfer (FRET) model. The rate constant for FRET (k_{ET}) can be expressed as:[47]

$$k_{ET} = \frac{9\ln(10)\,\kappa^2\Phi_{f(D)}}{128\pi^5 N_A n^4 \tau_D R_0{}^6}\,J \quad (1)$$

where κ^2, $\Phi_{f(D)}$, and J are the orientation factor (dimensionless), the luminescence quantum yield of the donor in the absence of acceptor (dimensionless), and spectral overlap (between the normalized donor emission area, and the Acceptor absorbance, unit L. $mol^{-1}.cm^{-1}.nm^4$), respectively. N_A and n are Avogadro's number (mol^{-1}) and the refractive index (dimensionless) of the medium, respectively. τ_D is the donor's fluorescence lifetime in the absence of the acceptor (ns). R_0 is the Förster distance (nm), which is the distance between donor (D) and acceptor (A) for 50% FRET efficiency. R_0 for a pair of D and A molecules is determined from parameters including $\Phi_{f(D)}$ and J, according to Equation (2):

$$R_0{}^6 = \frac{9\ln(10)\,\kappa^2\Phi_{f(D)}}{128\pi^5 N_A n^4}\,J \quad (2)$$

We determined R_0 values by analyzing the spectral overlaps between the host's PL and the absorbance of BTI-F as shown in Figure S17a (Supporting Information), and using the orientation factor κ^2 for polymeric media.[47b] The determined R_0 values for the LEC devices incorporating BTI-F and various host mixtures ranged from 1.1 to 3.9 nm, which are more broadly distributed than those observed for phenanthrene and anthracene derivatives in polymeric film (2.1–2.5 nm).[47b] Although the relationship is not perfectly linear, Figure S17b (Supporting Information) reveals a discernible trend indicating a correlation between the maximum electroluminescence of the LEC devices and their corresponding R_0 values. This suggests that the degree of spectral overlap is a crucial factor in the selection of an appropriate host for these LEC devices.

Consequently, the FT system is expected to show the best FRET and highest luminescence. However, low electroluminescence was obtained mainly due to unbalanced charge doping, resulting in uneven charge transport within the film. On the other hand, both CFT and the CVFT systems exhibited good overlap, in agreement with their high luminescence, while both single host systems (VT and CT) showed limited overlap with the absorbance of the guest, consistent with their modest observed efficiencies.

Attempts to correlate the PLQY of the host films to the luminescence and turn on voltage of the devices were not straightforward (Figure S18, Supporting Information). Systems with the high K_{ET} (BTI-F/CFT and BTI-F/CVFT) exhibited a high R^2 constant of 0.91 (vs luminescence) under pulsed current. However, the luminescence was not correlated to the quantum yield nor the current efficiency. This may be attributed to the overall LEC device performance being influenced by a combination of different factors, including charge injection, ion dynamics, device architecture, quenching processes, film morphology, and material stability.[16,48–52] While PLQY is an important parameter for understanding the potential luminescence efficiency within the active layer, it does not capture the full complexity of LEC device operation. Additionally, under operating conditions, photoluminescence begins to differ from electroluminescence, likely due to internal factors such as polaron-exciton interactions and Joule heating effects.[53]

Impedance spectroscopy was employed to i) investigate the influence of host materials on device resistance under applied DC voltage (0–6 V) and ii) estimate the electrical/ionic conductivity of the LEC cells (Figure S19, Supporting Information). The incorporation of p-CBP in the BTI-F/T system was found to significantly reduce the resistance and increase the electrical and ionic conductivity, indicating a favorable host-guest interaction. The resistance and behavior under applied current for the BTI-F/CVFT system fell between those of BTI-F/CFT and the BTI-F/CVT, revealing that there is a clear dependence of device efficiency on both ionic and electrical conductivities.

LECs function through the formation of a electric double layers (EDLs) at the electrode interfaces, followed by the electrochemical doping of the active layer, both of which are critical processes in LEC operation (Figure S20, Supporting Information). As illustrated in Figure S21 (Supporting Information), the impedance data for BTI-F in various host systems reveals a distinctive low-frequency capacitive behavior that is strongly influenced by the applied voltage in the 0–6 V range. This behavior is typical of LECs, as the applied bias causes ion migration toward the cathode (−) and anode (+), resulting in the formation of a p-i-n junction. Increasing voltage improves electrical conductivity through electrochemical doping. In BTI-F/CT single-host devices, a significant variation in electrical conductivity was observed due to the dual doping properties of p-CBP. Consequently, these devices exhibited the lowest resistance among the host systems tested; the resistance in BTI-F/CVFT was lower than that of BTI-F/CFT but higher than that of BTI-F/CVT (Figure S21k-o, Supporting Information).

Conductivity and capacitance were derived from equivalent circuit fitting of the impedance data (Figure S21p-t and S22, Supporting Information). In all systems, electrical conductivity increased with higher applied voltage, reflecting i) an increased density of charge carriers and ii) efficient electrochemical doping which facilitated effective charge carrier transport within the device.

In the host-free system (T), the capacitance of the electric double layer (CEDL) steadily decreased as the bias voltage increased. This reduction may be attributed to an unstable EDL layer, as the absence of a host material limits stabilization and impedes charge separation under the electric field.

Except for the CT system, introduction of a host resulted in an initial increase of the capacitance with applied bias up to ≈3–4 V, before showing a slight decrease. Applied bias facilitates the formation of the EDL, enhancing charge separation. The host materials in these systems likely contribute to stabilizing the EDL by providing stable structures for ion movement and accumulation. After reaching the 3–4 V threshold, the slight decrease in capacitance suggests that the EDL approaches a saturation point.

In the CT system, which contains the dual n and p type host p-CBP, the initial decrease in capacitance from 1 to 2 V may be attributed to the early stages of EDL formation. During this period, ions begin to migrate toward the electrodes but have not yet established an optimal charge distribution, leading to a temporary reduction in capacitance. p-CBP, with its ability to transport

both electrons and holes, may give rise to a more complex environment in which a temporary reduction in effective capacitance emerges as the system adjusts to the applied voltage and moves toward a quasi-equilibrium state, in which the EDL eventually becomes well-formed and balanced at voltages between 2 and 4 V. At higher voltages (>5 V), the p-CBP host might enhance charge carrier injection into the active layer, leading to greater ion accumulation at the EDL and an increase in capacitance. Overall, the presence of a host appears to contribute to stable EDL formation, which in turn may support the stability of the p-i-n junction.

Interestingly, the maximum luminance in the LECs correlates with ion resistance at 6 V but not at 0 V (Figure S22b, Supporting Information). This indicates that at 6 V, the LECs enter an active operational state, where the applied voltage is sufficient to trigger significant ion migration, with the formation of EDLs and doped regions at the electrode interfaces. In this state, ion resistance plays a critical role in determining how efficiently ions migrate, form EDLs, and facilitate charge injection into the emissive layer. As the ion resistance decreases, the formation of EDLs occurs more readily, improving charge injection and leading to higher luminance. This voltage-dependent relationship between luminance and ion resistance highlights the key role of EDL formation in device performance.

AFM images (Figure 5a; Figure S23, Supporting Information) were collected to investigate the surface homogeneity and assess how potential phase separation might impact device performance. In the absence of host materials, very rough surfaces were observed with a root-mean-square roughness (R_q) of 11.39 nm, revealing significant aggregation of BTI on the surface. After the addition of p-CBP, R_q decreased dramatically to 0.528 nm, indicating a much smoother surface. Optical images revealed small aggregated domains (0.5–1.5 µm) in the BTI-F/CT film, likely resulting from interactions between p-CBP and the fluorinated dye. The distinct differences in film morphology between BTI-F/CT and BTI-F/T highlight the critical role of p-CBP in interacting with BTI-F, effectively mitigating aggregation and the ACQ effect. Upon incorporation of PFO and PVK in the active layer, the surface roughness further decreased (R_q = 0.22 nm for PFO and 0.74 nm for PVK) and homogeneous surfaces were observed. The maze-like structure in the BTI-F/CFT likely arises from interactions between p-CBP and PFO. Given the continuous nature of the structure, where all points are linked in a chain without evidence of phase separation, it is likely that this structure provides percolation pathways, which facilitate charge transport and energy transfer processes. A similar maze-like structure was also observed in the CVFT systems, consistent with the interactions between PFO and p-CBP. However, the surface of these films appeared less homogeneous, characterized by an average roughness ($\mathbf{R_a}$) of *ca* 2.15 nm.

3. Conclusion

In this study, an unprecedented fluorinated benzothioxanthene imide (**BTI-F**) dye was synthesized and compared to its non-fluorinated parent in the context of LEC devices. Both dyes showed high thermal stability, high crystallinity, and good thin film processability. Upon incorporation in LEC devices, a high luminescence (≈3900 cd m^{-2}) was achieved using a dual host system, while high stability ($>t_{1/2}$ = 50 min) and extended switchability (>500 s) were demonstrated in triple host systems. This study sheds light on 4 key design principles that were exploited to achieve such outstanding results: i) a high spectral overlap of the guest's absorbance and hosts PL, ii) optimized energy band engineering to ensure smooth hole–electron traffic in LECs, iii) increased host-guest interactions, enhanced by F atom substitution, to suppress structure-induced ACQ and reduce the distance between the host-guest for high FRET efficiency, and iv) proper charge balance between n-type and p-type hosts in multi host-guest systems to increase luminescence, switchability and reduce the turn on voltage (V_{on}). Through these innovations, we realized the first example of multiple host LECs incorporating an entirely new class of guest based on the BTI structure. This study highlights the great potential of these metal-free fluorophores, while opening doors to new design principles and advanced device engineering using hosts in light emitting devices.

4. Experimental Section

Materials: PVK, PFO and THAB were used as received from Sigma Aldrich. 4,4′-Bis(9H-carbazol-9-yl) biphenyl (**p-CBP**) was purchased from TCI and used as received. Chlorobenzene was HPLC grade [Aldrich, >99% purity]. PEDOT: PSS and pattered ITO glass were purchased from Ossila and Wooyang GMS, respectively.

Synthesis of BTX Dyes: BTI was synthetized according to procedures previously reported by our group.[54] The synthesis of 2-amino-4-fluorobenzenethiol (2) was adapted from an early reported protocol.[20] Commercially available 5-fluoro-2-methylbenzo[d]thiazole (5 g, 1 eq) and sodium hydroxide (11.96 g, 10 eq) were placed into a 100 mL round bottom flask equipped with a condenser. Ethylene glycol (30 mL) and water (30 mL) were added, and the reaction mixture was stirred at 180 °C for 18 h. After cooling down to room temperature, the reaction mixture was diluted with water (50 mL) before being quenched with glacial acetic acid (≈100 mL) until the pH was slightly acidic. The resulting suspension was then extracted three times with diethyl ether and the organic phase was washed three times with water. After drying over magnesium sulfate and removal of the solvents in vacuo, 2 was obtained as a yellow oil (3.47 g, 81% yield) and used without further purification.

9-Fluoro-1H,3H-thioxantheno[2,1,9-def]isochromene-1,3-dione (**BTA-F**): 4-Bromo-1,8-naphthalic anhydride (2 g, 1 eq), potassium carbonate (499 mg, 0.5 eq) and 3 (1.14 g, 1.1 eq) were placed into a 100 mL round bottom flask. Dimethylformamide (50 mL) was added, and the reaction mixture was stirred at room temperature. After 24 h, TLC monitoring showed the disappearance of the starting material as well as the appearance of a new yellow spot attributed to the amine 4, which was not isolated. Isoamyl nitrite (2.90 mL, 3 eq) was then added to the reaction mixture and the temperature was increased to 60 °C. After 24 h, the mixture was poured into water and stirred for 5 min. The precipitates were filtered off and the resulting orange solid was thoroughly washed with water and a small portion of methanol. After drying under vacuum, BTA-F (1.41 g, 60% yield) was obtained as a bright orange solid and used without further purification. Due to insolubility in deuterated solvents, a complete 1H NMR scan was unable to perform. HRMS (EI) calculated for C18H7FO3S 322.0099, found 322.0105 ($\delta = -1.91$ ppm).

9-Fluoro-2-(pentan-3-yl)-1H-thioxantheno[2,1,9-def]isoquinoline-1,3(2H)-dione (BTI-F): BTA-F (1 g, 1 eq), pentan-3-amine (721 mL, 2 eq) and imidazole (5 g) were charged into a 50 mL round bottom flask equipped with a condenser. The reaction mixture was heated to 140 °C for 5 h. After cooling down to room temperature, the mixture was diluted in a 1 M aqueous HCl solution. The latter was extracted three times with dichloromethane. The organic phase was washed in sequence with 1 M HCl, water and brine before being dried over magnesium sulfate. After removal of the solvent in vacuo, the crude product was subjected to

a silica plug flash chromatography (eluent dichloromethane) to afford BTI-F as a bright orange solid (1.02 g, 85% yield). ^{1}H NMR (300 MHz, $CDCl_3$) δ 8.61 (d, J = 8.1 Hz, 1H), 8.42 (d, J = 8.0 Hz, 1H), 8.09 (d, J = 8.2 Hz, 1H), 7.90 (dd, J = 10.8, 2.6 Hz, 1H), 7.51 (d, J = 8.0 Hz, 1H), 7.35 (dd, J = 8.8, 5.5 Hz, 1H), 7.16 (ddd, J = 8.7, 7.3, 2.6 Hz, 1H), 5.13 – 4.97 (m, 1H), 2.24 (ddt, J = 14.8, 9.5, 7.4 Hz, 2H), 1.91 (tt, J = 13.4, 7.4 Hz, 2H), 0.89 (t, J = 7.5 Hz, 6H). ^{13}C NMR (75 MHz, CDCl3) δ 163.86, 160.60, 139.78, 135.62, 135.59, 130.67, 130.19, 130.09, 128.24, 128.13, 126.98, 126.94, 125.32, 120.64, 119.75, 118.22, 117.91, 112.92, 112.61, 57.54, 25.03, 11.46. 19F NMR (283 MHz, CDCl3) δ −112.81, −112.83, −112.85, −112.87, −112.89. HRMS (EI) calculated for $C_{23}H_{18}FNO_2S$ 391.1043, found 391.1047 (δ = −1.20 ppm).

Fabrication of LECs: For the host-less dyes/T approach, solutions of the active layer was prepared by dissolving dyes and THAB electrolyte at a mass ratio of 47:53 (1.05mg:1.18mg) in chlorobenzene. Noted that the weight of the dyes was fixed at 1.05 mg for all the active solutions to further eliminate the concentration effect of the dyes. For the single host dyes/CT approach, active solutions were mixed at a fixed weight ratio of dye:host:electrolyte at 18.3:61.0:20.6 in chlorobenzene. Meanwhile, for the dual-host system of dye/FCT and dye/CVT, the active solutions were prepared in a similar way at a ratio of dye:host1:host2:electrolyte = 15.9:53.0:13.1:17.8 and 18.7:62.6:15.6:0.03 using the same solvent. The electrolyte content was reduced to ≈3% in the dye/CVT system while maintaining all the weight content of remaining constituents to prevent the luminescence quenching effect caused by the over-doping of the ionic content. For the triple host dye/CVFT approach, the weight ratio was maintained as in the dye/CVT system while dividing the second host content into 2 equal parts, making the overall ratio as dye:host1:host2:host3:electrolyte = 18.7:62.6:7.8:7.8:0.03. Patterned ITO glass substrates were cleaned by ultrasonicating for 20 min in 600 mL of DI water and 3 g of Hellmanex III surfactant, followed by 20 min in DI water and finally 20 min in acetone. The substrates were then dried in an oven at 80 °C for at least 1 h to remove any solvent residues before undergoing a UV–ozone treatment for 20 min. PEDOT: PSS (35 nm) was spin-coated on the substrates at 4000 rpm for 60 s before baking at 110 °C for 1 h. The substrates were then transferred into a dry N_2-filled glovebox. The active layers were then spin-coated at 2000 rpm for 60 s and annealed for 1 h at 70 °C. Finally, a set of four Al (100 nm) electrodes was deposited on top of the active material by thermal evaporation under high vacuum (1×10^{-5} Pa) through a shadow mask.

Instruments and Characterization: For the voltage-driving method (**VPL**), the voltage was fixed using a Keithley 2400 sourcemeter and increase by 0.1 V every 2 s, controlled by the program. For the pulsed current method (**PCL**), the current (235 Hz, 50% duty cycle) was generated by a Keithley 2400 sourcemeter controlled by a MATLAB code. The voltage, luminescence, and EL spectra (380–780 nm) of the LEC were measured upon application of ramped current and were recorded using a Konica Minolta CS-2000 spectroradiometer. TGA, DSC and DTA were measured through a simultaneous TGA/DSC SDT Q600 (manufactured by TA Instrument). Absorption and fluorescence spectra of thin films and solutions were measured using a Perkin-Elmer lambda 750 spectrophotometer and a Konica Minolta CS-2000 spectroradiometer, respectively (with excitation at 365 nm from a UV lamp). The thickness of the PEDOT:PSS and the active layer were measured with a stylus profilometer (Bruker, DektakXT). The thickness of active layer for BTI-F based LECs in different host system was measured using SEM as 64.7, 67.4, 97.5, 112.6, and 84.8 nm for BTI-F/T, BTI-F/CT, BTI-F/CVT, BTI-F/CFT, and BTI-F/CVFT, respectively. Cyclic voltammetry experiments were conducted at a concentration of 1×10^{-3} M under an inert atmosphere in a standard one-compartment, three-electrode electrochemical cell using a Biologic ESP-300 potentiostat equipped with a 1 A/48 V booster and a linear scan generator. Tetrabutylammonium perchlorate (**TBAP**) was used as the supporting electrolyte (0.1 M) in anhydrous dichloromethane. The vitreous carbon (∅ = 3 mm) working electrodes were polished with diamond paste before each recording. A platinum wire counter electrode was used. The Ag^+/Ag reference electrode was made of a silver wire immersed in a solution containing a known concentration of Ag^+ ($AgNO_3$ (10^{-2} M) + tetrabutylammonium perchlorate (0.1 M) in acetonitrile). The HOMO and LUMO energy level was calculated from the oxidation (reduction) onset as

$$E_{HOMO}\ (eV) = -\left(4.8\,eV + eV_{ox,onset,Fc/Fc^+}\right) \quad (3)$$

$$E_{LUMO}\ (eV) = -\left(4.8\,eV + eV_{red,onset,Fc/Fc^+}\right) \quad (4)$$

Supporting Information

Supporting Information is available from the Wiley Online Library or from the author.

Acknowledgements

The authors sincerely thank Bright Walker (Kyung Hee University) for the valuable discussions and insightful comments on this manuscript. This research was supported by a National Research Foundation (NRF) grant funded by Korean government (Ministry of Science, ICT Future Planning, MSIP) through the Global Research Lab (GRL: 2016K1A1A2912753) and Creative Materials Discovery Program (2018M3D1A1058536 and RS-2023-00302697). D. P. S. and K.M. acknowledge the MITI of the CNRS and the ANR (BTXI-Apogee, ANR-20-CE05-0029), respectively. This study also received the support of the EUR LUMOMAT (programme Investissements d'Avenir ANR-18-EURE-0012).

Conflict of Interest

The authors declare no conflict of interest.

Author Contributions

K.K.L. and H.K. contributed equally to this work. K.K.L., H.K., J.K., Y.A., and D.K. performed Thin film characterization, device fabrication and testing. K.M., P.J., and D.S. performed synthesis of active compounds and structural characterization. P.B. performed supervision and discussion. C.M. performed discussion and co-writing. C.C. and E.K. performed supervision, co-PIs, co-writing and funders of this projects.

Data Availability Statement

The data that support the findings of this study are available from the corresponding author upon reasonable request.

Keywords

benzothioxanthene imide, fluorescent materials, host/guest, organic grid material, organic light-emitting electrochemical cells

Received: June 26, 2024
Revised: October 8, 2024
Published online: October 24, 2024

[1] S. B. Meier, D. Tordera, A. Pertegas, C. Roldan-Carmona, E. Orti, H. J. Bolink, *Mater. Today* **2014**, *17*, 217.
[2] H. C. Su, H. F. Chen, C. C. Wu, K. T. Wong, *Chem. –Asian J.* **2008**, *3*, 1922.

[3] L. He, L. Duan, J. Qiao, R. Wang, P. Wei, L. Wang, Y. Qiu, *Adv. Func. Mater.* **2008**, *18*, 2123.
[4] K. P. S. Zanoni, M. S. Sanematsu, N. Y. M. Iha, *Inorg. Chem. Commun.* **2014**, *43*, 162.
[5] N. Demir, M. Karaman, G. Yakali, B. Gultekin, T. Tugsuz, S. Denizalti, S. Demic, M. Aygun, B. Dindar, M. Can, *ACS Appl. Elec. Mater.* **2020**, *2*, 3549.
[6] B. N. Bideh, H. Shahroosvand, M. K. Nazeeruddin, *Inorg. Chem.* **2021**, *60*, 11915.
[7] R. D. Costa, F. J. Cespedes-Guirao, E. Ortí, H. J. Bolink, J. Gierschner, F. Fernandez-Lazaro, A. Sastre-Santos, *Chem. Commun.* **2009**, *26*, 3886.
[8] Z. B. Hill, D. B. Rodovsky, J. M. Leger, G. P. Bartholomew, *Chem. Commun.* **2008**, *48*, 6594.
[9] A. Pertegás, D. Tordera, J. J. Serrano-Pérez, E. Ortí, H. J. Bolink, *J. Am. Chem. Soc.* **2013**, *135*, 18008.
[10] M. D. Weber, J. E. Wittmann, A. Burger, O. B. Malcıoğlu, J. Segarra-Martí, A. Hirsch, P. B. Coto, M. Bockstedte, R. D. Costa, *Adv. Funct. Mater.* **2016**, *26*, 6737.
[11] M. Mone, S. Tang, P. Murto, B. A. Abdulahi, C. Larsen, J. Wang, W. Mammo, L. Edman, E. Wang, *Chem. Mater.* **2019**, *31*, 9721.
[12] K. T. Weber, K. Karikis, M. D. Weber, P. B. Coto, A. Charisiadis, D. Charitaki, G. Charalambidis, P. Angaridis, A. G. Coutsolelos, R. D. Costa, *Dalton Trans.* **2016**, *45*, 13284.
[13] M. S. Subeesh, K. Shanmugasundaram, C. D. Sunesh, Y. S. Wonb, Y. Choe, *J. Mater. Chem. C* **2015**, *3*, 4683.
[14] P. Lundberg, E. M. Lindh, S. Tang, L. Edman, *ACS Appl. Mater. Interfaces* **2017**, *9*, 28810.
[15] P. Lundberg, Y. Tsuchiya, E. M. Lindh, S. Tang, C. Adachi, L. Edman, *Nat. Commun.* **2019**, *10*, 5307.
[16] S. Kanagaraj, A. Puthanveedu, Y. Choe, *Adv. Funct. Mater.* **2020**, *30*, 1907126.
[17] L. A. Galán, J. M. A. Castán, C. Dalinot, P. S. Marqués, P. Blanchard, O. Maury, C. Cabanetos, T. Le Bahers, C. Monnereau, *Phys. Chem. Chem. Phys.* **2020**, *22*, 12373.
[18] L. A. Galán, J. M. A. Castán, C. Dalinot, P. S. Marqués, J. Galiana, P. Blanchard, C. Andraud, E. Dumont, O. Maury, C. Cabanetos, C. Monnereau, T. Le Bahers, *J. Phys. Chem. B* **2021**, *125*, 8572.
[19] D. P. Sánchez, P. Josse, N. Plassais, G. Park, Y. Khan, Y. Park, M. Seinfeld, A. Guyard, M. Allain, F. Gohier, L. Khrouz, D. Lungerich, H. S. Ahn, B. Walker, C. Monnereau, C. Cabanetos, T. Le Bahers, *Chem. –Eur. J.* **2024**, *30*, 202400191.
[20] M. Deiana, J. M. A. Castán, P. Josse, A. Kahsay, D. P. Sánchez, K. Morice, N. Gillet, R. Ravindranath, A. K. Patel, P. Sengupta, I. Obi, E. Rodriguez-Marquez, L. Khrouz, E. Dumont, L. A. Galán, M. Allain, B. Walker, H. S. Ahn, O. Maury, P. Blanchard, T. Le Bahers, D. Öhlund, J. von Hofsten, C. Monnereau, C. Cabanetos, N. Sabouri, *Nucleic Acids Res.* **2023**, *51*, 6264.
[21] M. Deiana, P. Josse, C. Dalinot, A. Osmolovskyi, P. S. Marqués, J. M. A. Castán, L. A. Galán, M. Allain, L. Khrouz, O. Maury, T. Le Bahers, P. Blanchard, S. Dabos-Seignon, C. Monnereau, N. Sabouri, C. Cabanetos, *Commun. Chem.* **2022**, *5*, 142.
[22] D. P. Sánchez, K. Morice, M. G. Mutovska, L. Khrouz, P. Josse, M. Allain, F. Gohier, P. Blanchard, C. Monnereau, T. Le Bahers, N. Sabouri, Y. Zagranyarski, C. Cabanetos, M. Deiana, *J. Mater. Chem. B* **2024**, *12*, 8107.
[23] S. K. Serviou, P. L. Gkizis, D. P. Sánchez, N. Plassais, F. Gohier, C. Cabanetos, C. G. Kokotos, *ChemSusChem* **2024**, 202400903.
[24] J. M. A. Castán, C. Amruth, P. Josse, L. A. Galan, P. S. Marqués, M. Allain, O. Maury, T. Le Bahers, P. Blanchard, C. Monnereau, G. C. Welch, C. Cabanetos, *Mater. Chem. Front.* **2022**, *6*, 1912.
[25] K. Youssef, Y. Li, S. O'Keeffe, L. Li, Q. Pei, *Adv. Func. Mater.* **2020**, *30*, 1909102.
[26] S. Tang, A. Sandström, P. Lundberg, T. Lanz, C. Larsen, S. van Reenen, M. Kemerink, L. Edman, *Nat. Commun.* **2017**, *8*, 1190.
[27] S. Tang, W.-Y. Tan, X.-H. Zhub, L. Edman, *Chem. Commun.* **2013**, *49*, 4926.
[28] S. Tang, H. A. Buchholz, L. Edman, *J. Mater. Chem. C* **2015**, *3*, 8114.
[29] M. Rémond, J. Hwang, J. Kim, S. Kim, D. Kim, C. Bucher, Y. Bretonnière, C. Andraud, E. Kim, *Adv. Funct. Mater.* **2020**, *30*, 2004831.
[30] S. Tang, A. Sandström, P. Lundberg, T. Lanz, C. Larsen, S. van Reenen, M. Kemerink, L. Edman, *Nat. Commun.* **2017**, *8*, 1190.
[31] S. Tang, C. Larsen, J. Ràfols-Ribé, J. Wang, L. Edman, *Adv. Opt. Mater.* **2021**, *9*, 2002105.
[32] J. M. A. Castán, C. Dalinot, S. Dayneko, L. A. Galan, P. S. Marqués, O. Alévêque, M. Allain, O. Maury, L. Favereau, P. Blanchard, G. C. Welch, C. Cabanetos, *Chem. Commun.* **2020**, *56*, 10131.
[33] Gaussian 09, M. Frisch, G. Trucks, H. Schlegel, G. Scuseria, M. Robb, J. Cheeseman, G. Scalmani, V. Barone, B. Mennucci, G. Petersson, H. Nakatsuji, M. Caricato, X. Li, H. Hratchian, A. Izmaylov, J. Bloino, G. Zheng, J. Sonnenberg, M. Hada, M. Ehara, K. Toyota, R. Fukuda, J. Hasegawa, M. Ishida, T. Nakajima, Y. Honda, O. Kitao, H. Nakai, T. Vreven, J. Montgomery, et al., Gaussian Inc Wallingford CT **2016**.
[34] C. Yao, Y. Zhu, K. Gu, J. Zhao, J. Ning, D. F. Perepichka, Y.-L. Loo, H. Meng, *J. Mater. Chem. A* **2020**, *8*, 12149.
[35] M. Adeel, M. Khalid, M. A. Ullah, S. Muhammad, M. U. Khan, M. N. Tahir, I. Khan, M. Asghar, K. S. Mughal, *RSC Adv.* **2021**, *11*, 7766
[36] U. Resch-Genger, Y. Q. Li, J. L. Bricks, V. Kharlanov, W. Rettig, *J. Phys. Chem. A* **2006**, *110*, 10956.
[37] B. Hua, C. Zhang, W. Zhou, L. Shao, Z. Wang, L. Wang, H. Zhu, F. Huang, *J. Am. Chem. Soc.* **2020**, *142*, 16557.
[38] T. M. Figueira-Duarte, P. G. Del Rosso, R. Trattnig, S. Sax, E. J. List, K. Müllen, *Adv. Mater.* **2010**, *22*, 990.
[39] T. Zhang, Y. Liang, J. Cheng, J. Li, *J. Mater. Chem. C* **2013**, *1*, 757
[40] B. Chen, J. Ding, L. Wang, X. Jing, F. Wang, *J. Mater. Chem.* **2012**, *22*, 23680.
[41] J. Mucelini, I. Østrøm, A. O. Ortolan, K. F. Andriani, G. F. Caramori, R. L. Parreira, K. K. Laali, *Dalton Trans.* **2019**, *48*, 13281.
[42] R. D. Lunn, D. A. Tocher, P. J. Sidebottom, M. G. Montgomery, A. C. Keates, C. J. Carmalt, *Cryst. Growth Des.* **2021**, *21*, 3024.
[43] T. Glaser, S. Beck, B. Lunkenheimer, D. Donhauser, A. Köhn, M. Kröger, A. Pucci, *Org. Electronics* **2013**, *14*, 575.
[44] T. Sakanoue, J. Li, H. Tanaka, R. Ito, S. Ono, S. I. Kuroda, T. Takenobu, *Adv. Mater.* **2017**, *29*, 1606392.
[45] M. Di Marcantonio, F. Vollkommer, G. Bacher, E. Nannen, *J. Mater. Chem. C* **2018**, *6*, 9742.
[46] C. Lin, P. Chen, Z. Xiong, D. Liu, G. Wang, Y. Meng, Q. Song, *Nanotechnology* **2018**, *29*, 075203
[47] a) R. M. Clegg, *Lab. Tech. Biochem. Mol. Biol.* **2009**, *33*, 1. b) R. S. Roller, M. A. Winnik, *J. Phys. Chem. B* **2005**, *109*, 12261.
[48] J. Xu, A. Sandström, E. M. Lindh, W. Yang, S. Tang, L. Edman, *ACS Appl. Mater. Interfaces* **2018**, *10*, 33380.
[49] J. Mindemarkab, L. Edman, *J. Mater. Chem. C* **2016**, *4*, 420.
[50] K. Sato, S. Uchida, S. Toriyama, S. Nishimura, K. Oyaizu, H. Nishide, Y. Nishikitani, *Adv. Mater. Tech.* **2017**, *2*, 1600293.
[51] E. M. Lindh, P. Lundberg, T. Lanz, L. Edman, *Sci. Report* **2019**, *9*, 10433.
[52] M. Alahbakhshi, A. Mishra, R. Haroldson, A. Ishteev, J. Moon, Q. Gu, J. D. Slinker, A. A. Zakhidov, *ACS Energy Lett.* **2019**, *4*, 2922.
[53] K. Yoshida, H. Nakanotani, C. Adachi, *Org. Electronics* **2016**, *31*, 287.
[54] P. Josse, K. Morice, D. P. Sánchez, T. Ghanem, J. Boixel, *New J. Chem.* **2022**, *18*, 8393.